SAR Sentinel Data Analysis: Hydrological Dynamics and Rainfall Patterns in the Kampar River Basin (2018-2023)

Husnul Kausarian[1,*], Josaphat Tetuko Sri Sumantyo[2], Batara[3], Adi Suryadi[1], Thio Pangestu[1]

[1]Engineering Geological Program, Faculty of Engineering, Universitas Islam Riau, Indonesia

[2]Center for Environmental Remote Sensing, Chiba University, Japan

[3]State Key Laboratory of Marine Geology and School of Ocean and Earth Science, Tongji University, Shanghai, China

*Author to whom correspondence should be addressed:
Email: husnulkausarian@eng.uir.ac.id

(Received March 13, 2024; Revised September 2, 2024; Accepted September 11, 2024).

Abstract: This study investigates the hydrological dynamics and rainfall patterns in the Kampar River Basin from 2018 to 2023 using Synthetic Aperture Radar (SAR) data from Sentinel-1. The analysis reveals significant year-to-year variations in annual rainfall, with 2019 exhibiting notably low intensity, aligning with classifications from the Indonesian Meteorological, Climatological, and Geophysical Agency (BMKG). The months from September to December consistently experience higher rainfall, contributing to increased water volumes and flood risks in the river basin. Using ArcMap 10.3 software, the flood extent was mapped based on Sentinel-1 imagery, identifying recurring flood-prone areas in Pekanbaru and Kampar, particularly during peak rainfall periods. This spatial analysis, combined with rainfall data, offers a comprehensive view of flood dynamics in the region. The study also incorporates interferometric SAR analysis to explore land surface deformations, revealing patterns of land subsidence despite challenges such as atmospheric conditions and vegetation interference. These findings underscore the need for integrated approaches that consider climatic, hydrological, and geophysical factors to enhance flood risk mitigation strategies. The study demonstrates the utility of SAR data in detecting and analyzing hydrological patterns, contributing to the understanding of environmental changes in the Kampar River Basin and offering valuable insights for future research and practical applications in the field of hydrology.

Keywords: Kampar River; SAR Sentinel Data; Geospatial Analysis; Rainfall Patterns; Interferogram Processing

1. Introduction

Indonesia, with its archipelagic landscape and diverse geographical features, faces recurrent natural disasters, particularly floods. Among the numerous river systems in the country, the Kampar River basin in Sumatra stands out due to its complex interplay of geographical and meteorological factors, making it highly susceptible to flooding[1,2]. Understanding and managing flood-prone areas within this basin is crucial for safeguarding lives, property, and ecosystems.

The Kampar River, spanning approximately 413 kilometers, originates in the Bukit Barisan mountain range and flows through Riau Province before discharging into the Malacca Strait. The river is vital for regional agriculture, industry, and local livelihoods. However, this importance is overshadowed by the river's vulnerability to flooding, exacerbated by factors such as climate change, deforestation, and land-use changes. The Kampar River basin's proximity to the equator presents unique challenges for flood risk management. The equatorial climate brings high rainfall levels, leading to significant fluctuations in river discharge. Moreover, the region experiences atmospheric turbulence and elevated water vapor, complicating satellite-based flood monitoring. These challenges necessitate the use of advanced technologies to accurately assess flood risks[3,4].

To enhance the accuracy of flood identification, this research integrates six years of rainfall data (2018-2023) from the Indonesian Meteorological, Climatological, and Geophysical Agency (BMKG). By correlating this rainfall data with SAR imagery, the study aims to elucidate the complex hydrological processes within the Kampar River basin, offering insights into the temporal and spatial patterns of flooding[5–7].

The primary objectives of this research are to identify and delineate flood-prone areas along the Kampar River, analyze rainfall patterns, and establish correlations

between these patterns and flood occurrences. Achieving these objectives will contribute valuable information to flood risk assessment and management strategies in the region[8–11].

The findings of this research are anticipated to have significant implications for disaster preparedness and mitigation efforts. By improving the understanding of flood dynamics in the Kampar River basin, the study supports the development of early warning systems and targeted interventions, thereby reducing the impact of floods on local communities and ecosystems. Additionally, the integration of SAR Sentinel data with rainfall information provides a comprehensive view of the interactions between meteorological events and hydrological processes, enhancing the effectiveness of flood risk management strategies[12].

2. Geological and Research Background

The study focuses on the Kampar River Basin, situated in the Riau Province, Indonesia. Geographically located between 0.9° N to 1.7° S latitude and 100.5° E to 102.0° E longitude, the Kampar River Basin is a critical hydrological region in the heart of Sumatra (Fig. 1). This region is characterized by a tropical climate, marked by high temperatures and substantial rainfall throughout the year.

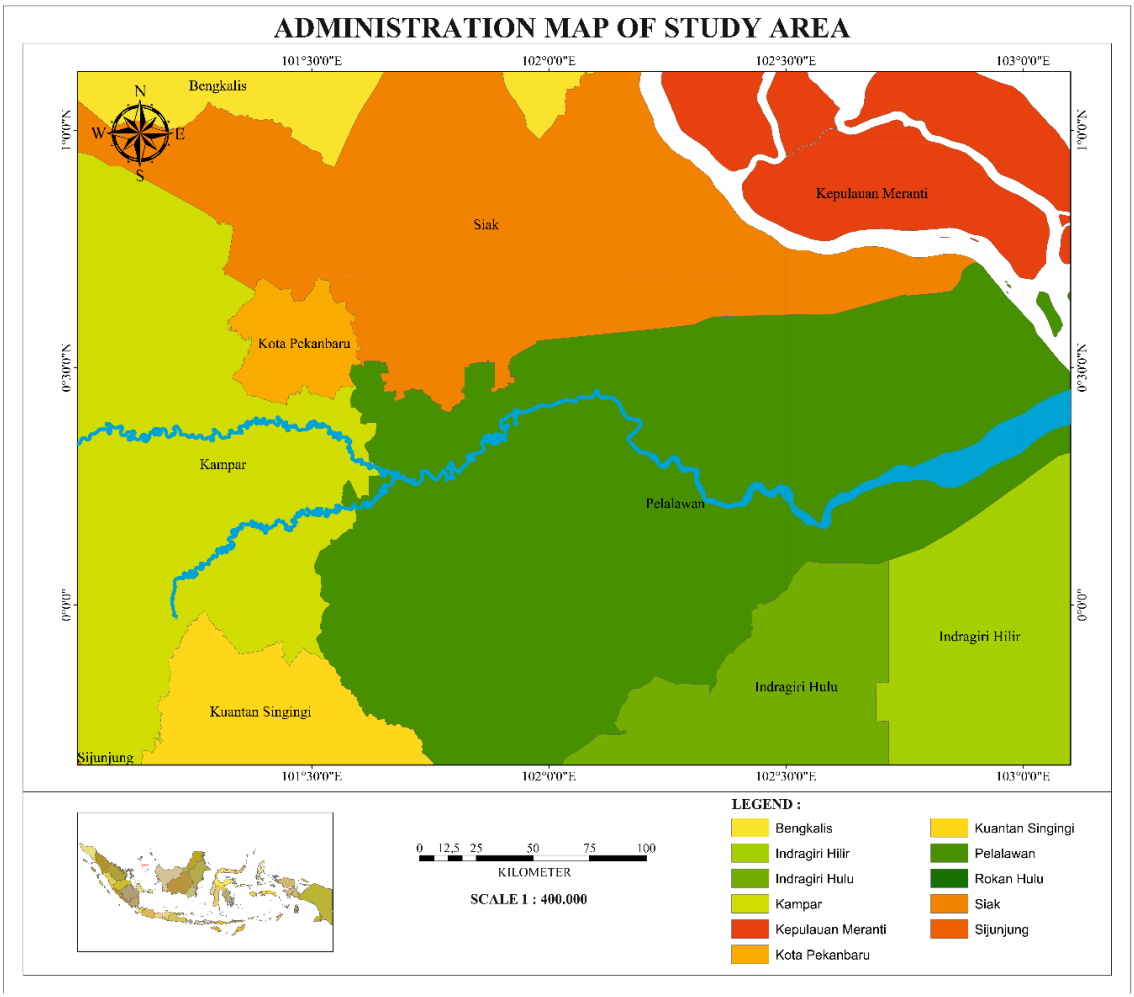

Fig. 1: Administration map of study area Kampar River (Source: database Riau Government).

Administratively, the river spans across several districts, constituting a critical area for hydrological studies, particularly in flood identification and management. The primary administrative divisions within the study area include the districts of Pekanbaru, Kampar, and several sub-districts such as Langgam, Bandar Sei Kijang, Pangkalan Kerinci, and Pangkalan Kuras. Pekanbaru, serving as the provincial capital of Riau, holds a central position in the administrative landscape of the region.

Kampar, one of the prominent districts in Riau, encompasses diverse land uses, ranging from urbanized areas to extensive plantations and forests. This administrative unit is of particular interest due to its vulnerability to flooding, influenced by factors such as land cover characteristics, topography, and rainfall patterns. The sub-districts, including Langgam, Bandar Sei Kijang, Pangkalan Kerinci, and Pangkalan Kuras, contribute significantly to the spatial dynamics of the

Kampar River Basin. These areas exhibit varying degrees of urbanization and land use, influencing the hydrological characteristics and flood susceptibility of the region. The Kampar River Basin, with its intricate administrative structure, provides an ideal setting for understanding the complex interplay of environmental factors leading to floods. By delving into the administrative nuances of the study area, this research aims to contribute valuable insights into flood management and risk reduction strategies tailored to the specific characteristics of the Kampar River.

3. Synthetic Aperture Radar (SAR) in Earth Observation

Synthetic Aperture Radar (SAR) is commonly employed for mapping the Earth's surface and terrain. Traditionally, SAR finds applications in military and commercial domains[13] (Fig. 2). It is a type of active non-optical remote sensing system designed to overcome the limitations of the Real Aperture Radar (RAR) system. RAR utilized increasingly longer antennas to achieve higher resolution. SAR methods produce high-resolution radar image data, particularly in azimuth resolution. The spatial resolution of the radar system is influenced by microwave radiation and geometric effects[14,15] (Table 1). In SAR, two main spatial resolutions exist: range resolution, dependent on the pulse length generated by the radar sensor, and azimuth resolution, determined by the angular width of the microwave radiation sensing the Earth's surface and the slant range distance (CCRS, 2014).

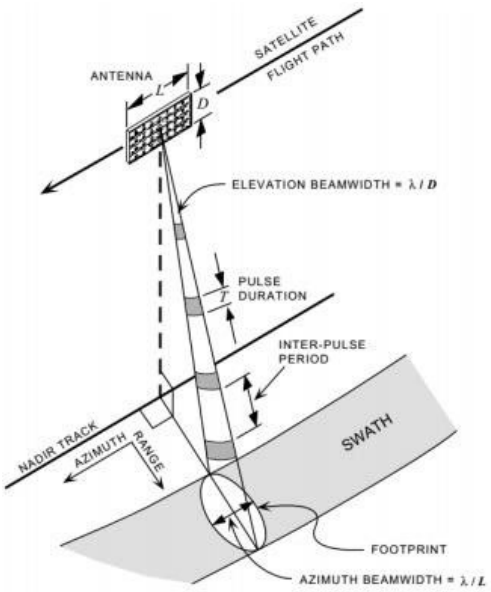

Fig. 2: Synthetic Aperture Radar (Zalite and Voormansik, 2016).

SAR represents a collection of two-dimensional pixels in slant range (r) and azimuth (x). Each pixel corresponds to a small part of the Earth's surface, termed a resolution cell. These pixels contain complex numbers representing the phase and amplitude information of the backscattered signal from objects on the Earth's surface. Phase information is obtained from two SAR image data in interferometric form, while amplitude information indicates the backscattering capability (backscatter). The spatial resolution of SAR is influenced by the size of the antenna used in the system. Longer antennas result in better spatial resolution. Other factors affecting SAR spatial resolution include pulse duration (r), antenna beamwidth (β), and look angle ($\theta 1$)[14,16].

Table 1. Frequency and Wavelength of SAR Systems (Zalite et al., 2014).

Band	Wavelength (cm)	Frequency (GHz)	SAR System
X	3.1	9.6	TanDEM-X, COSMO-Skymed
C	5.6	5.4	Sentinel-1, Radarsat-2
L	23.5	1.3	ALOS PALSAR 2
P	70.0	0.4	BIOMASS

4. Sentinel-1 Satellite

The Sentinel-1 satellite, the first designed and developed by the European Commission (EC) and the European Space Agency (ESA), carries a C-band SAR sensor for Earth surface observation at a frequency of 5.405 GHz, providing rapid data acquisition. The C-band SAR can operate in both single-polarization and dual-polarization modes, depending on the observation mode. Sentinel-1 has four observation modes: Strip Map (SM), Interferometric wide-swath (IW), Wave mode (WV), and Extra wide-swath (EW). The Interferometric Wide-swath (IW) mode, the primary operational mode over land, provides Level-1 SLC (Single Look Complex) and GRDH (Ground Range Detected High) data with a spatial resolution of 5m x 20 m and a wide coverage of 250 km. Operating in dual polarization (HH+HV, VV+VH), IW mode captures detailed information (Table 2). Sentinel-1 consists of two satellites, Sentinel-1A and Sentinel-1B, launched in 2014 and 2016, respectively, with a mission lifespan of 7 to 12 years[7,17,18]. The Sentinel-1 mission is geared towards monitoring Earth's surface (forests, water, soil, agriculture), disaster mitigation, marine monitoring, oil spill mapping, and climate change monitoring (ESA, 2012).

Table 2. Sentinel-1 Satellite Characteristics of Kampar River (ESA, 2012).

Parameter	Interferometric Wide-Swath mode (IW)	Wave mode (WV)	Strip Map mode (SM)	Extra Wide-Swath mode (EW)
Polarisation	Dual (HH+HV, VV+VH)	Single (HH, VV)	Dual (HH+HV, VV+VH)	Dual (HH+HV, VV+VH)
Incidence Angle	310 - 460	230 + 370	(mid-incidence angle)	200 - 470
Azimuth Resolution	20 m	5 m	5 m	40 m
Ground Range Resolution	5 m	5 m	5 m	20 m
Swath	250 km	20 x 20 km	80 km	410 km
Maximum noise-equivalent sigma zero (NESZ)	-22 dB	-22 dB	-22 dB	-22 dB
Radiometric Stability	0.5 dB	0.5 dB	0.5 dB	0.5 dB
Radiometric Accuracy	1 dB	1 dB	1 dB	1 dB
Phase Error	50	50	50	50

4.1 Preparation Stage

The preparatory phase represents the initial step in the research process, involving the collection of Sentinel-1A radar data, ASTER GDEM V3 data, administrative boundary data for Kampar River, and river basin maps for Kampar River. Sentinel-1 radar data is obtained from the Copernicus Open Access Hub, with a GRD (Ground Range Detector) sensor mode IW (Interferometric Wide-swath) dual polarization (VV+VH), acquired on December 21, 2019, and January 2, 2020. ASTER GDEM V3 data is sourced from NASA's Earthdata Search portal[19]. Administrative boundary data for Kampar River is acquired from the BIG Ina-geoportal in shapefile format. River basin maps for Kampar River are obtained from the Environmental and Forestry Agency (DLHK) of Kampar River. The preparatory phase represents the initial step in the research process, involving the collection of Sentinel-1A radar data, ASTER GDEM V3 data, administrative boundary data for Kampar River, and river basin maps for Kampar River. Sentinel-1 radar data is obtained from the Copernicus Open Access Hub, with a GRD (Ground Range Detector) sensor mode IW (Interferometric Wide-swath) dual polarization (VV+VH), acquired on December 21, 2019, and January 2, 2020. ASTER GDEM V3 data is sourced from NASA's Earthdata Search portal. Administrative boundary data for Kampar River is acquired from the BIG Ina-geoportal in shapefile format. River basin maps for Kampar River are obtained from the Environmental and Forestry Agency (DLHK) of Kampar River.

4.2 Digital Processing Stage

The processing of Sentinel-1 radar imagery involves digital remote sensing image interpretation in two stages: pre-processing and processing. Pre-processing includes subset image processing, multilooking, radiometric calibration, geometric calibration, and linear to/from dB conversion. Processing involves stacking pre-flood and post-flood images, RGB compositing, and random forest classification to derive flood distribution maps. SNAP software is used for Sentinel-1 data processing, and ArcGIS 10.3 is employed to obtain flood distribution maps.

The initial step in image processing is the subset process, aiming to limit the coverage of the research area. Multilooking is conducted to reduce speckle and image dimensions for faster processing. Radiometric calibration is a process to obtain backscatter sigma naught values. Sigma naught is a coefficient obtained from the backscatter correction component of the image, sensitive to the region's topography. Subsequently, geometric correction is applied to adjust the image coordinates to the Earth coordinate system. The range-doppler terrain correction is employed to transform Sentinel-1 image geometry from radar geometry to the Earth coordinate system, aligning it with field coordinates. Finally, Linear to/from dB conversion is carried out to convert backscatter sigma naught values to decibel units.

The processing stage starts by stacking pre-flood and post-flood images using stack tools in SNAP software to create a single image from December 21, 2019, and January 2, 2020. The stacked image is then composited into RGB to facilitate the differentiation between permanent water bodies, non-flood areas, and flood areas. The RGB result displays various colors, subsequently classified into two categories: flood and non-flood areas using supervised random forest classification (Table 3). The processed Sentinel-1 image is reclassified using ArcGIS software to convert the raster-formatted image into polygons. The flood polygons are then overlaid with the research area boundaries to determine the extent of flood inundation in each sub-district within the study area.

The processing to generate slope, elevation, and river flow pattern maps is achieved by extracting information from ASTER GDEM V3 data. The ASTER GDEM V3 image is cropped based on the administrative boundaries of the research area. The DEM, containing elevation data, undergoes spatial analysis for slope maps and hydrological analysis for river flow pattern maps[20–22]. For elevation maps, a reclassification based on height classes with a 5-meter interval is performed. The overlay method

is applied to elevation and slope data with flood distribution data.

Table 3. RGB Band Composite.

Band	Image
Red	Sigma naught pre-flood image
Green	Sigma naught post-flood image
Blue	Sigma naught post-flood image

The analysis of the relationship between topographic factors and flood extent is based on slope and elevation, and the correlation level between these two variables is determined using the Pearson correlation coefficient (r)[23–26] (Table 4).

Hydrological processing involves the steps of fill, flow direction, flow accumulation, con, and stream. The fill step is conducted to fill empty cells (pixels). Its purpose is to modify the values of cells with higher elevations than others, allowing trapped water to flow. Flow direction is employed to obtain the flow direction based on the grid from the DEM. This step provides the slope values of each cell. Flow accumulation indicates the accumulation result of the flow in each cell by accumulating the weight of each cell flowing towards the upstream. The result of flow accumulation is a river network. The con step is carried out to determine the threshold on the river network from the flow accumulation results. Subsequently, stream order is applied to indicate the order of each river network using the Strahler method. The river basin map of Kampar River obtained from DLHK is rectified (georeferenced) to align spatial data on the map with precise coordinates. After the rectification process, digitization is performed to obtain river basin boundary polygons in the study area.

4.3 Data Analysis

Data analysis applied to Sentinel-1 radar data involves using random forest classification to generate flood distribution maps in the Kampar River based on the flood disaster in January 2020. Random Forest classification is applied to the composited RGB image, combining pre-flood and post-flood sigma naught values.

The random forest classification results in flooded areas displayed in red, non-flood areas in gray, and permanent water bodies in dark black. Spatial analysis is performed on ASTER GDEM V3 imagery to produce topographic maps of the Kampar River area, including slope, elevation, and river flow pattern maps. Descriptive quantitative analysis is then applied to analyze the relationship between slope, elevation, river flow patterns, and flood distribution. The slope map is classified according to the classes in Table 5, while the elevation map is classified as shown in Table 6. The correlation between slope and elevation is assessed using the Pearson correlation coefficient (r).

Table 4. Pearson Correlation Coefficient Analysis (Naidu et al., 2018).

Interval	Coefficient	Relationship Level
0.00–0.19	Very low	Very low correlation
0.20–0.39	Low	Low correlation
0.40–0.59	Moderate	Moderate correlation
0.60–0.79	Strong	Strong correlation
0.80–1.00	Very strong	Very strong correlation

Table 5. Slope Classification (Directorate General Regulation No P.4/V-SET/2013).

Class	Slope Range
Flat	< 8
Gentle	8 – 15
Moderate	15 – 25
Steep	25 – 40

Table 6. Elevation Classification.

No	Elevation Range (m.dpal)
1	< 5
2	5–10
3	10 – 15
4	15 – 20
5	20 – 25
6	25 – 30
7	30 – 35
8	35 – 40
9	> 40

Morphometric aspects of a river basin applied include river order patterns, river branching ratio (Rb). River order in this study is determined using the Strahler method[27,28]. Once river orders are obtained, the value of the river branch ratio, indicating the characteristics of the rise and fall of a river's flow, can be determined.

5. Results and Analysis

5.1 Rainfall Processing Data

Flood processing data can be derived from rainfall data obtained from BMKG. This observation was conducted from 2018 to 2023 along the Kampar River. The analysis focuses on understanding the rainfall data around the Kampar River.

The observed rainfall data for the Kampar River in Riau from 2018 to 2023 indicates significant differences from year to year (Fig. 3 and 4). The data for each year is presented below:

Table 7. Rainfall Data for Kampar River in 2018-2023.

Year	Time Interval (Months)	Duration	Average Rainfall
2018	01 – 12	365 Days	435.5076735
2019	01 – 12	365 Days	559.597478
2020	01 – 12	366 Days	429.0587286
2021	01 – 12	365 Days	277.2398938
2022	01 – 12	365 Days	436.1803014
2023	01 – 12	304 Days	129.5040098

Table 8. Rainfall Data for Pekanbaru in 2018-2023.

Year	Time Interval (Months)	Duration	Average Rainfall
2018	01 – 12	365 Days	819.8452129
2019	01 – 12	365 Days	547.8273135
2020	01 – 12	366 Days	832.7905867
2021	01 – 12	365 Days	575.1468753
2022	01 – 12	365 Days	689.7411403
2023	01 – 12	304 Days	1417.338226

5.2 Rainfall Values

The rainfall values ($z > 0.2$) are ideal for accurately depicting the phase information. A correlation value less than 0.1 provides less effective phase information. The absence of correlation is also known as decorrelation and can occur between two pairs of SAR images taken at different times. Low coherence values may result from factors such as differences in scattering strength and distribution, known as temporal decorrelation. Variables influencing this include plant growth, weather, and recording intervals. Additionally, other factors that can degrade coherence values are spatial decorrelation due to spatial baseline effects (distance between two orbits) and volume scattering[29].

The processed Rainfall Values for Kampar and Pekanbaru show annual values, indicating the vulnerability to floods. The values range from highly prone to floods to not prone to floods. Further discussions and interpretations will be conducted based on these values to understand the implications for flood susceptibility in the studied areas.

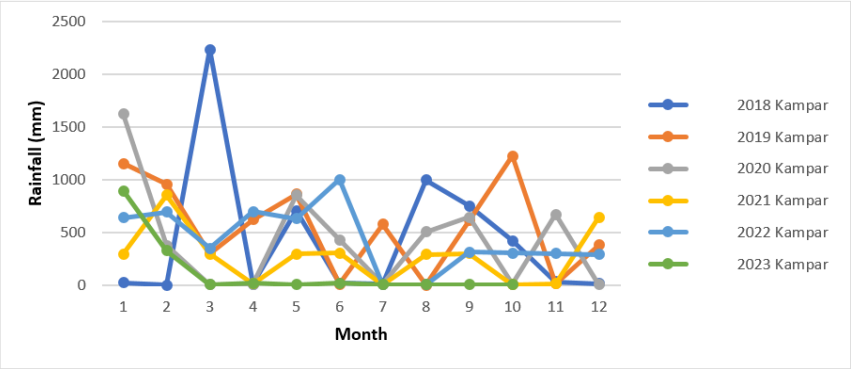

Fig. 3: Rainfall Graph in Kampar (2018-2023).

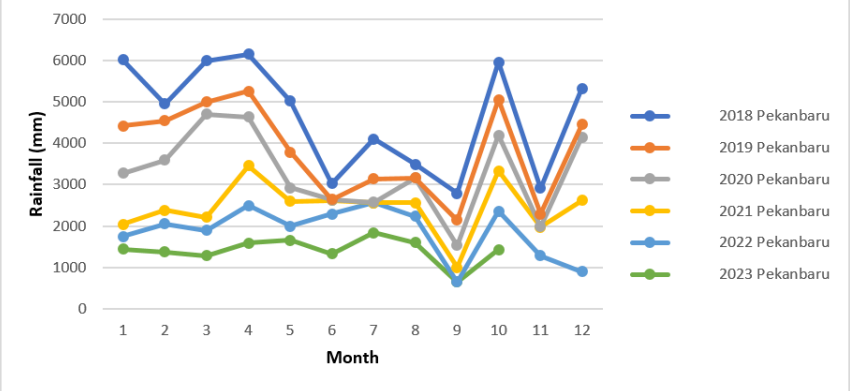

Fig. 4: Rainfall Graph in Pekanbaru (2018-2023).

5.3 Relationship between Rainfall and Watershed (DAS) Rainfall Values

The data on rainfall reveals that from 2018 to 2023, the average rainfall in the river basin area is known. Rainfall significantly influences the watershed discharge in the Kampar River, as evident from the graphical representation of the past six years. The data illustrates that the high monthly average rainfall occurs typically from September to December. During these months, the high rainfall intensity affects the water volume in the Kampar River Watershed.

When there is high-intensity rainfall, the smaller tributaries (orders) in the watershed get filled, and the

water continues to flow towards the downstream of the larger watershed. This larger watershed has the capacity to accommodate a substantial amount of rainfall. Consequently, the river discharge increases, resulting in diverse flow patterns within this watershed.

Watersheds with numerous tributaries, both on the left and right sides of the main river, face an increased risk of flooding during periods of high rainfall. This is because the meeting points of the smaller tributaries with the main river, known as confluences, can experience flooding due to varying volumes or discharges produced by different order tributaries. Therefore, the probability of flooding is heightened in these areas during high rainfall, leading to dynamic and varied river discharges in the watershed.

5.4 Calculating Flooded Area

In this stage, the flooded area is calculated using ArcMap 10.3 software. The Sentinel-1 image data is transformed from raster (pixels) to vector (lines) using the "raster to polygon" command. The outcomes of the raster-to-polygon process are displayed in Fig. 5.

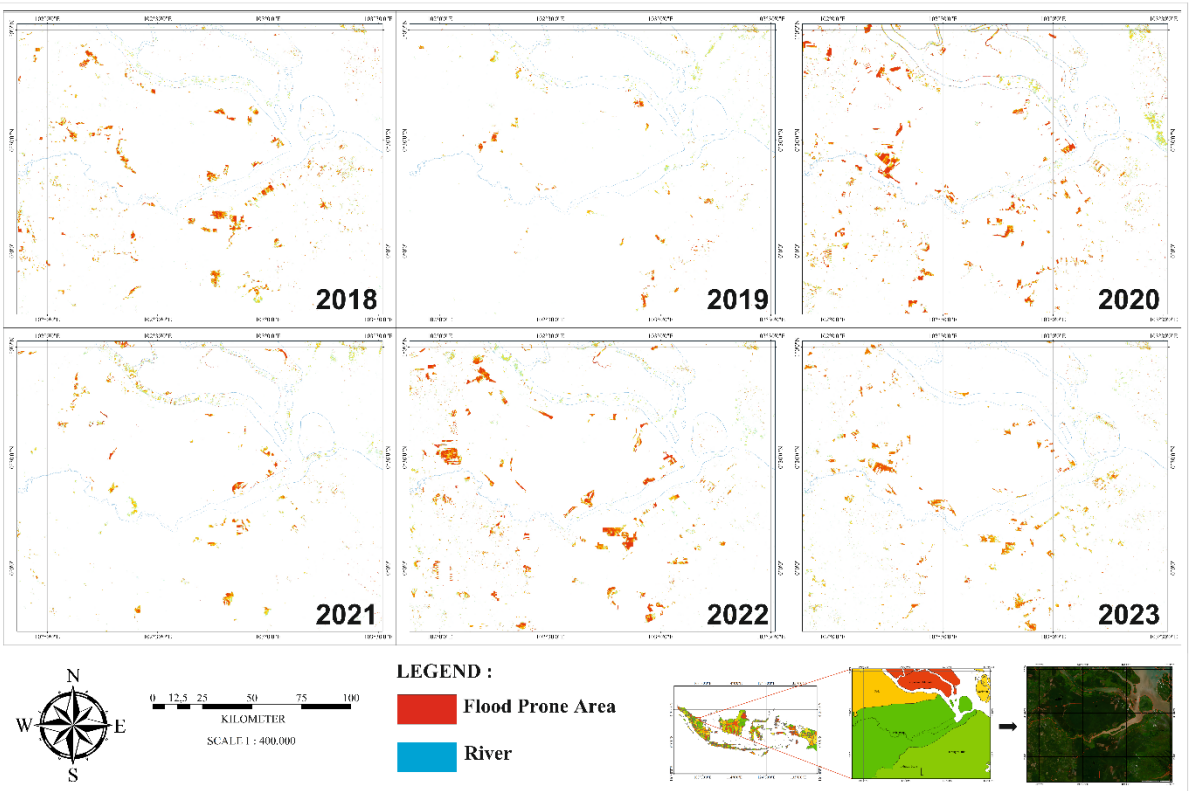

Fig. 5: Illustrates the spatial distribution of flood-prone areas surrounding the Kampar River from 2018 to 2023.

Following this, the "calculate geometry" process is implemented to automatically compute the flooded area based on the geometrical shapes of the data and the coordinate system used.

The identification of flooded areas in Sentinel-1 images is executed using ArcMap 10.3 software by calculating the extent of the flood-affected region. The results of identifying the flood distribution that occurred in Pekanbaru and Kampar from 2018 to 2023 are presented.

This process enables the determination of the spatial extent of the flood, providing valuable information for understanding the impact of flooding in the region. The combination of raster-to-polygon conversion and geometry calculation ensures an accurate and comprehensive analysis of the flooded areas, aiding in effective flood management and mitigation strategies.

5.5 Interferogram of Image Pairs

The wavelength of the Sentinel 1-A sensor (C-Band) is relatively low compared to the L-Band sensor. This makes C-Band images less applicable in areas with high vegetation (rural areas) (Taekuchi, 2002). Sentinel-1A (C-Band) images cannot penetrate trees, causing the signal to be mostly reflected from the top of the canopy, with minimal reflection from the trunks (Zhou, 2013). The atmospheric conditions in the research area, an equatorial region, significantly affect the presence of noise effects and orbits, which can reduce the quality of SAR data and complicate the unwrapping process. Noise in the interferogram image can result from temperature systems, overlays, or inconsistencies during the splicing process (Qing, 2011). The SAR interferogram is generated by cross-multiplying each pixel of the first (master) SAR image with the

corresponding pixel of the second (slave) SAR image. The amplitude of the interferogram is the amplitude of the master image multiplied by the slave image, and the phase produced is the phase difference between the two images (European Space Agency (ESA), 2007).

From the interferogram results, image pairs in the research area do not show any significant changes in the form of apparent fringes. This indicates no noticeable changes due to deformation phenomena typically observed in volcanic eruptions or earthquakes.

5.6 Filtered Interferogram Results

The filtering process aims to increase the Signal-to-Noise Ratio (SNR) contained in the interferogram phase. This step is performed to eliminate noise in the interferogram image caused by signal propagation back to the air or atmosphere and noise due to temporal decorrelation effects or orbit errors that degrade the quality of the interferogram image. The purpose of this process is to enhance accuracy and sharpen the formed phase and fringes. Fringes result from the phase gradient formed by SAR image pairs.

The outcome of this process will yield an image with radar coordinates in radians. It still contains ambiguity caused by image information ranging from -π to +π (high phase value jumps). To remove this ambiguity, a phase unwrapping process is necessary.

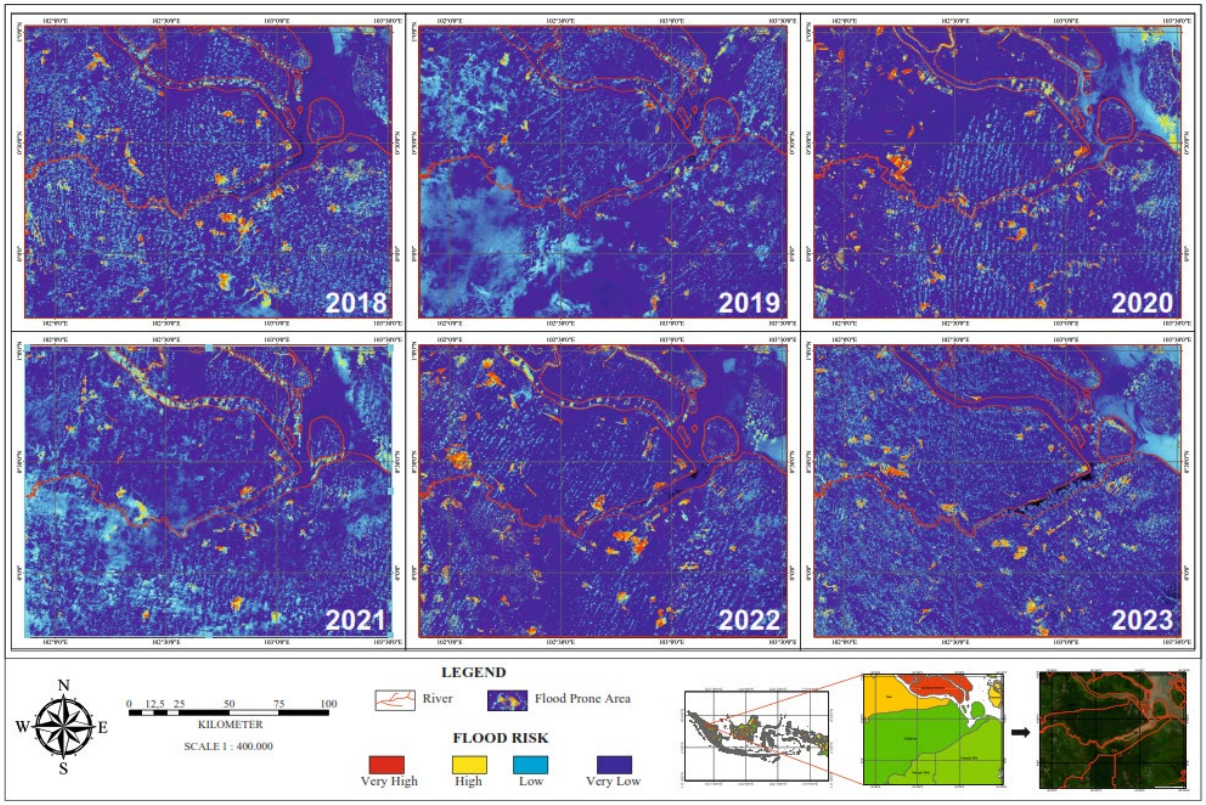

Fig. 6: Illustrates the interferogram results after filtering for a pair of images from the years 2018 to 2023, showcasing the spatial distribution of flood-prone areas surrounding the Kampar River.

5.7 Analysis of Discontinuities in Land Surface Subsidence Patterns

Discontinuities in land surface subsidence patterns in Pekanbaru and Kampar can result from various factors originating from satellite vehicles or environmental conditions. Some factors indicated as causes of these discontinuities include:

This influences recorded data due to evaporation activity in the troposphere layer, which is relatively high in the equatorial region. This is a drawback in InSAR technology, particularly in repeat-pass InSAR applications, as electromagnetic waves experience delays when passing through atmospheric layers (especially troposphere and ionosphere).

The research area is one with high vegetation density, primarily composed of swamp forests covering around 641,801.97 hectares (BPS, 2017). Discontinuities, especially in the eastern part of the research area, may be caused by the dominance of plantation areas. High vegetation areas have a higher chance of experiencing high temporal decorrelation due to the rapid plant growth in those regions.

Discontinuities appearing in the research area are mostly in regions between the patches of two IW SAR images. Differences in IW and scene image conditions can cause discontinuities due to variations in recording time related to differences in atmospheric conditions in the research area. Additionally, differences in incidence angle

and off-nadir angle/look angle between each IW can be a factor influencing the appearance of discontinuities.

6. Conclusion

The comprehensive analysis conducted in this study reveals critical insights into the hydrological dynamics and land surface deformations in the Kampar River area from 2018 to 2023. By systematically examining data from Sentinel SAR, BMKG rainfall records, geological maps, and DEM data, the study identifies significant annual variations in rainfall, with notable high rainfall periods from September to December impacting river basin discharge and contributing to flood risks. The spatial analysis using ArcMap 10.3 software provided a detailed visualization of flood patterns in Pekanbaru and Kampar, enhancing our understanding of flood dynamics in the region.

Additionally, interferometric SAR analysis highlighted patterns of land subsidence despite challenges from atmospheric conditions and vegetation interference. The study underscores the importance of integrated approaches considering climatic, hydrological, and geophysical factors to better understand and mitigate the region's vulnerability to floods and land surface deformations. These findings offer valuable information for developing future flood management and adaptation strategies in the Kampar River area.

Acknowledgements

The authors would like to thank all who supported this research activity, especially the Government of Kampar District and the Government of Riau Province, for supporting the provision of secondary data. Furthermore, the authors would like to thank Universitas Islam Riau, Chiba University, Japan, and State Key Laboratory of Marine Geology and School of Ocean and Earth Science, Tongji University, Shanghai, China, who continue to support the research collaborations, especially the Geological Engineering Program, Universitas Islam Riau.

References

1) Y. Yuskar, D.B.E. Putra, and M. Revanda, “Quarternary sediment characteristics of floodplain area: study case at kampar river, rumbio area and surroundings, riau province,” J. Geosci. Eng. Environ. Technol., 3 (1) 63 (2018). doi:10.24273/jgeet.2018.3.1.1226.
2) Z.W. Kundzewicz, S. Kanae, S.I. Seneviratne, J. Handmer, N. Nicholls, P. Peduzzi, R. Mechler, L.M. Bouwer, N. Arnell, K. Mach, R. Muir-Wood, G.R. Brakenridge, W. Kron, G. Benito, Y. Honda, K. Takahashi, and B. Sherstyukov, “Flood risk and climate change: global and regional perspectives,” Hydrol. Sci. J., 59 (1) 1–28 (2014). doi:10.1080/02626667.2013.857411.
3) H. Kausarian, A. Suryadi, Susilo, Batara, and J.T.S. Sumantyo, “Flood problem in pekanbaru city analysis using gis approach,” J. Phys. Conf. Ser., 1783 (1) 012090 (2021). doi:10.1088/1742-6596/1783/1/012090.
4) C. Wulandari, “Identifying climate change adaptation efforts in the batutegi forest management unit, indonesia,” For. Soc., 48–59 (2021). doi:10.24259/fs.v5i1.7389.
5) H. Kausarian, Lady Redyafry, Josaphat Tetuko Sri Sumantyo, A. Suryadi, and Muhammad Zainuddin Lubis, “Structural analysis of the central sumatra basin using geological mapping and landsat 8 oli/tirs c2 l1 data,” Evergreen, 10(2) 792–804 (2023). doi:10.5109/6792830.
6) M. Whittle, S. Quegan, Y. Uryu, M. Stüewe, and K. Yulianto, “Detection of tropical deforestation using alos-palsar: a sumatran case study,” Remote Sens. Environ., 124 83–98 (2012). doi:10.1016/j.rse.2012.04.027.
7) K. Koppel, K. Zalite, A. Sisas, K. Voormansik, J. Praks, and M. Noorma, “Sentinel-1 for urban area monitoring — Analysing local-area statistics and interferometric coherence methods for buildings’ detection,” in: 2015 IEEE Int. Geosci. Remote Sens. Symp. IGARSS, IEEE, Milan, Italy, 2015: pp. 1175–1178. doi:10.1109/IGARSS.2015.7325981.
8) T. Carlà, P. Farina, E. Intrieri, K. Botsialas, and N. Casagli, “On the monitoring and early-warning of brittle slope failures in hard rock masses: examples from an open-pit mine,” Eng. Geol., 228 71–81 (2017). doi:10.1016/j.enggeo.2017.08.007.
9) S. Naidu, K.S. Sajinkumar, T. Oommen, V.J. Anuja, R.A. Samuel, and C. Muraleedharan, “Early warning system for shallow landslides using rainfall threshold and slope stability analysis,” Geosci. Front., 9 (6) 1871–1882 (2018). doi:10.1016/j.gsf.2017.10.008.
10) Irma Alfie Yassin, R. Patrisina, and E. Amrina, “Location-allocation model for victims and health workers during post earthquake-tsunami health crisis in padang city,” Evergreen, 9(1) 234–245 (2022). doi:10.5109/4774244.
11) A. Arunika, Jaka Fajar Fatriansyah, and Venia Andira Ramadheena, “Detection of asphalt pavement segregation using machine learning linear and quadratic discriminant analyses,” Evergreen, 9(1) 213–218 (2022). doi:10.5109/4774236.
12) Z. Wang, D. Wang, Q. Guo, and D. Wang, “Regional landslide hazard assessment through integrating susceptibility index and rainfall process,” Nat. Hazards, 104 (3) 2153–2173 (2020). doi:10.1007/s11069-020-04265-5.
13) K. Zalite, K. Voormansik, J. Praks, O. Antropov, and M. Noorma, “Towards detecting mowing of agricultural grasslands from multi-temporal

COSMO-SkyMed data," in: 2014 IEEE Geosci. Remote Sens. Symp., IEEE, Quebec City, QC, 2014: pp. 5076–5079. doi:10.1109/IGARSS.2014.6947638.
14) A. Ferretti, G. Savio, R. Barzaghi, A. Borghi, S. Musazzi, F. Novali, C. Prati, and F. Rocca, "Submillimeter accuracy of insar time series: experimental validation," IEEE Trans. Geosci. Remote Sens., 45 (5) 1142–1153 (2007). doi:10.1109/TGRS.2007.894440.
15) M. Muslihudin, Wiwiek Rabiatul Adawiyah, E. Hendarto, Ratri Damaryanti Megasari, and Muhammad Fadil Ramadhan, "Environmental constraints in building process a sustainable geothermal power plant on the slopes of slamet mount, central java, indonesia," Evergreen, 9(2) 300–309 (2022). doi:10.5109/4793669.
16) A. Ferretti, C. Prati, and F. Rocca, "Permanent scatterers in sar interferometry," IEEE Trans. Geosci. Remote Sens., 39 (1) 8–20 (2001). doi:10.1109/36.898661.
17) C.M.M. Kittel, L. Jiang, C. Tøttrup, and P. Bauer-Gottwein, "Sentinel-3 radar altimetry for river monitoring – a catchment-scale evaluation of satellite water surface elevation from sentinel-3a and sentinel-3b," Hydrol. Earth Syst. Sci., 25 (1) 333–357 (2021). doi:10.5194/hess-25-333-2021.
18) S.S. Dagne, H.H. Hirpha, A.T. Tekoye, Y.B. Dessie, and A.A. Endeshaw, "Fusion of sentinel-1 sar and sentinel-2 msi data for accurate urban land use-land cover classification in gondar city, ethiopia," Environ. Syst. Res., 12 (1) 40 (2023). doi:10.1186/s40068-023-00324-5.
19) N. Arifian, K.R. Denis, and S.K. Putri, "COMPARISON of aster gdem images and srtm images for river watershed and geomorphology study," Int. Remote Sens. Appl. J., 3 (2) 68–73 (2023). doi:10.24036/irsaj.v3i2.38.
20) H. Kausarian, A. Suryadi, - Susilo, J.T.S. Sumantyo, and - Batara, "GIS analysis for flood problem in the big city: a case study in pekanbaru city, riau province, indonesia," Int. J. Adv. Sci. Eng. Inf. Technol., 11 (1) 342 (2021). doi:10.18517/ijaseit.11.1.11974.
21) A. Yussupov and Raya Z. Suleimenova, "Use of remote sensing data for environmental monitoring of desertification," Evergreen, 10(1) 300–307 (2023). doi:10.5109/6781080.
22) M.Z. Lubis, G. Surya, D.S. Pamungkas, B. Subhan, H.M. Manik, H. Kausarian, and W. Anurogo, "Characteristics of waters during transitional season, senimba waters," Trends Sci., 19 (11) 4495 (2022). doi:10.48048/tis.2022.4495.
23) Y. Izumi, J. Widodo, H. Kausarian, S. Demirci, A. Takahashi, P. Razi, M. Nasucha, H. Yang, and J. Tetuko S. S., "Potential of soil moisture retrieval for tropical peatlands in indonesia using alos-2 l-band full-polarimetric sar data," Int. J. Remote Sens., 40 (15) 5938–5956 (2019). doi:10.1080/01431161.2019.1584927.
24) H. Kausarian, J.T. Sri Sumantyo, D.B. eka Putra, A. Suryadi, and G. Gevisioner, "Image processing of alos palsar satellite data, small unmanned aerial vehicle (uav), and field measurement of land deformation," Int. J. Adv. Intell. Inform., 4 (2) 132 (2018). doi:10.26555/ijain.v4i2.221.
25) M. Rahman, C. Ningsheng, G.I. Mahmud, M.M. Islam, H.R. Pourghasemi, H. Ahmad, J.M. Habumugisha, R.M.A. Washakh, M. Alam, E. Liu, Z. Han, H. Ni, T. Shufeng, and A. Dewan, "Flooding and its relationship with land cover change, population growth, and road density," Geosci. Front., 12 (6) 101224 (2021). doi:10.1016/j.gsf.2021.101224.
26) G. Shen, W. Fu, H. Guo, and J. Liao, "Water body mapping using long time series sentinel-1 sar data in poyang lake," Water, 14 (12) 1902 (2022). doi:10.3390/w14121902.
27) M. Feng, K. Jung, and J.-C. Kim, "Geomorphologic analysis of small river basin within the framework of fractal tree," Water, 12 (9) 2480 (2020). doi:10.3390/w12092480.
28) Mohammed Ali Berawi, A. Darmawan, Gunawan, P. Miraj, and Hamzah Abdul Rahman, "Land value capture: defining crucial variables difference-in-differences model for residential properties surrounding mrt jakarta stage i," Evergreen, 7(2) 253–261 (2020). doi:10.5109/4055228.
29) C.-H. Lu, C.-F. Ni, C.-P. Chang, J.-Y. Yen, and R. Chuang, "Coherence difference analysis of sentinel-1 sar interferogram to identify earthquake-induced disasters in urban areas," Remote Sens., 10 (8) 1318 (2018). doi:10.3390/rs10081318.